Generation of two-dimensional chaotic vector fields from a surface-emitting semiconductor laser: Analysis of vector singularities

C. C. Chen, K. W. Su, T. H. Lu, C. C. Liu, Y. F. Chen,* and K. F. Huang

Department of Electrophysics, National Chiao Tung University, Hsinchu, Taiwan

(Received 2 May 2007; revised manuscript received 28 June 2007; published 30 August 2007)

We demonstrate experimental generation of two-dimensional (2D) chaotic vector fields from a surface-emitting microcavity laser with precisely control of the operating temperature and the operating current. The 2D optical vector field is found to be formed by frequency locking of two linearly polarized laser modes with different chaotic spatial structures. The eigenfunction expansion method is used to reconstruct the experimental wave function for analyzing the properties of the vector singularities. It is shown that the distribution of vector singularities obeys the sign rule of nearest-neighbor singularities in the phase space of the vector field.

PACS number(s): 42.25.Ja, 03.65.−w, 42.60.Jf, 42.55.Sa

I. INTRODUCTION

The quantum-billiard model is often used as a paradigm to study the quantum properties corresponding to classical chaotic systems [1]. Berry proposed that the statistical properties of high-lying energy eigenstates of classically chaotic systems can be generally described by a superposition of numerous plane waves of fixed wave-vector magnitude but random amplitude, phase, and direction [2]. Using numerical analyses, the two-dimensional (2D) chaotic wave functions have been found to exhibit the spatial patterns of quasilinear structures [3–5]. In addition to quantum chaos, the quantum-billiard model is also employed to investigate electron transport phenomena in mesoscopic quantum systems [6,7]. It has been perceived that the conductance fluctuations in quantum dots are intimately associated with the quantum wave functions localized on classical trajectories [8–11]. This finding indicates that the study of the morphology of wave functions proffers specific insight into experimental quantities in mesoscopic quantum systems.

The spatial properties of high-order wave functions have been experimentally investigated with analogous wave systems including microwave cavities [1,12–15], acoustic resonators [16,17], optical fibers [18], optical systems [19], and microcavity lasers [20–23]. In particular, optical coherent fields not only can be utilized to visualize the morphology of wave functions in confined systems but also can be employed to manifest polarization singularities because of their vector nature [24–26]. The study of polarization singularities is one significant category of singular optics that is a very modern area of interest in contemporary physics [27]. There are two types of singularity of the polarization vectors of paraxial optical beams: vector singularity and Stokes singularities [28]. Vector singularities are isolated, stationary points in a plane at which the orientation of the electric vector of a linearly polarized vector field becomes undefined. The features of vector singularities have been experimentally observed in laser modes with the interrelated behavior of spatial structures and polarization states [29–34]. However,

so far all experimental demonstrations have been related to the eigenmodes of integrable optical cavities; no experiments have demonstrated explicitly the entanglement of polarization and spatial structures in chaotic laser resonators.

In this work, we fabricate a square-shaped vertical cavity surface-emitting laser (VCSEL) with a moderate ripple boundary to generate 2D chaotic vector fields by precisely controlling the operating temperature and operating current. The experimental results reveal that each vector field consists of two linearly polarized laser modes with different chaotic spatial structures, but synchronized to a single frequency. To show the properties of vector singularities, we use the eigenfunction expansion technique to reconstruct the wave function for two orthogonal-polarization near-field patterns. With the reconstructed wave functions, the distribution of vector singularities is clearly found to obey the sign rule of nearest-neighbor singularities in the phase space of the vector field [35]. More importantly, it is confirmed that phase extrema are hardly visible in 2D chaotic vector fields.

II. GENERATION OF POLARIZATION-ENTANGLED 2D CHAOTIC VECTOR FIELDS

In this investigation, a square-shaped oxide-confined VC-SEL with a moderate ripple boundary was developed to be a
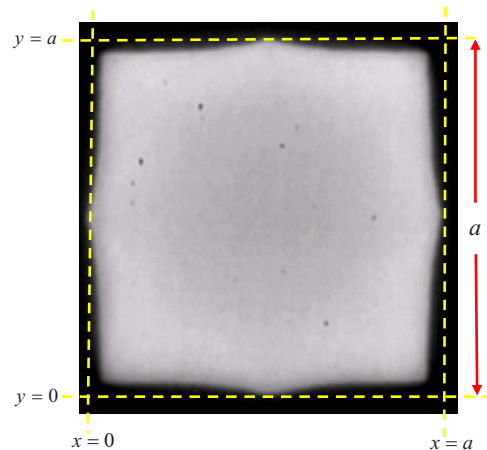

FIG. 1. (Color online) Experimental pattern of the spontaneous emission showing details of the ripple boundary.

*Corresponding author. Fax: (886-35) 729134. yfchen@cc.nctu.edu.tw

laterally confined nonintegrable system [22]. Figure 1 shows the pattern of the spontaneous emission that manifests the details on the ripple boundary. The forms for the bottom and top walls of the ripple are approximately expressed as

$$Y(x) = \begin{cases} 0.044a\left[1 - \exp\left(-13.5\left|\dfrac{x}{a} - \dfrac{1}{2}\right|\right)\right] & \text{for the bottom wall,} \\ a - 0.044a\left[1 - \exp\left(-13.5\left|\dfrac{x}{a} - \dfrac{1}{2}\right|\right)\right] & \text{for the top wall,} \end{cases} \tag{1}$$

where a is the central length of the ripple boundary. The right and left walls of the ripple are described with the same functional form. The structure of this oxide-confined VCSEL is shown in Fig. 2(a). The size of the oxide aperture is 45 $\times 45$ μm^2.

Although the transverse confinement of the VCSEL device has been successfully demonstrated to be like a 2D wave billiard system [20–23], the fundamental operation is summarized here in order to make the representation self-contained and to give our notation. The function of the 2D wave billiard wall in the VCSEL device comes from the fact that the large index discontinuity between the oxide layer and surrounding semiconductor leads to a total internal reflection of a wave incident upon the boundary. The separability of the wave function in the VCSEL device enables the wave vectors to be decomposed into k_z and k_t, where k_z is the
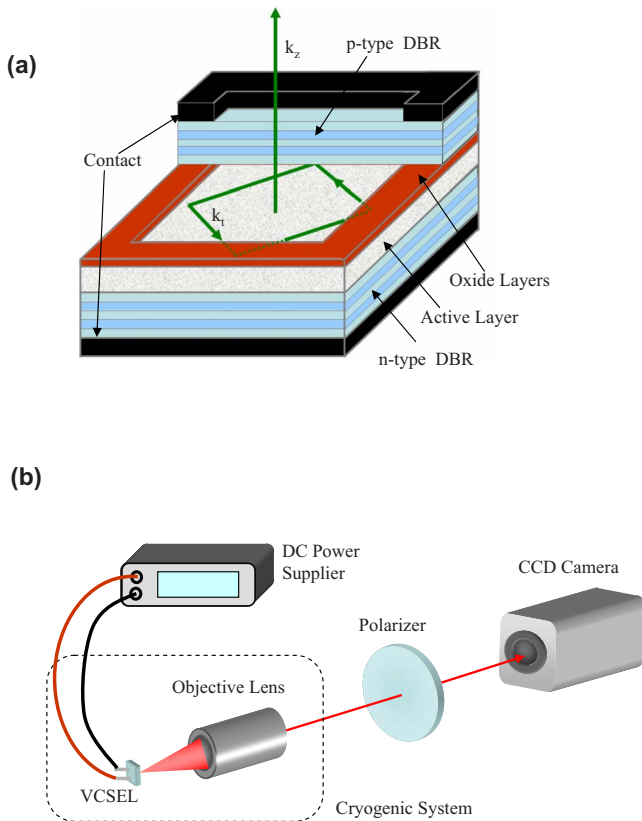

(a)

(b)

FIG. 2. (Color online) (a) Basic structure of the surface-emitting microcavity laser. (b) Experimental configuration for generation of 2D chaotic vector fields.

wave-vector component along the direction of vertical emission and k_t is the transverse wave-vector component. The vertical dimension of the cavity is designed to have a large k_z component and a relatively small transverse component k_t, generally $k_t < 0.12k_z$. The angle between the photon velocity vector and the normal vector of the boundary surface, $\tan^{-1}(k_z/k_t)$, can be calculated to be greater than 1.45 rad. On the other hand, the critical angle for total reflection is given by $\sin^{-1}(n_{ox}/n_{GaAs})$, where n_{ox} is the effective refractive index of the oxide layer and n_{GaAs} that of the semiconductor cavity. With $n_{ox} \approx 1.54$ and $n_{GaAs} \approx 3.5$, it can be confirmed that the angle between the photon velocity vector and the normal vector of the boundary surface is certainly greater than the critical angle for total reflection. As a consequence, the lateral oxide boundaries can be modeled as rigid walls and the losses through the wall boundaries are extremely low.

Under the circumstance of paraxial optics, $k_t \ll k_z$, the longitudinal field is significantly small in comparison with the transverse field. Therefore, the electric field can be approximated as having only transverse components and no longitudinal component, i.e., so-called quasi-TEM waves. After separating the z component in the wave equation, we are left with a two-dimensional Helmholtz equation $(\nabla_t^2 + k_t^2)\psi(x,y) = 0$, where ∇_t^2 is the Laplacian operator operating on the coordinates in the transverse plane and $\psi(x,y)$ is a scalar wave function that describes the transverse distribution of the laser mode. As a result, the transverse eigenfunctions of the oxide-confined VCSEL device are equivalent to the eigenfunctions of the 2D Schrödinger equation with hard wall boundaries of the same geometry. The vertical cavity is formed by two distributed Bragg reflectors (DBRs) and its optical length is designed to be nearly one wavelength (806.5 nm). Since the vertical emission through the top DBR represents the coupling of the wave field from the inside cavity to the outside environment, the phasor amplitude of the emission field distribution $E(x,y,z)$ can be expressed as $E(x,y,z) = \psi(x,y)e^{-jk_z z}$. More importantly, the transverse near-field wave patterns can be straightforwardly reimaged from the surface-emitting laser output.

The experimental setup is shown in Fig. 2(b). The VCSEL device was placed in a cryogenic system with a temperature stability of 0.01 K in the range 80–270 K. A current source with a precision of 0.01 mA was utilized to drive the VCSEL device. The near-field patterns were reimaged into a charge-coupled device (CCD) camera (Coherent, Beam-Code) with a microscope (Mitsutoyo, numerical aperture 0.9). A polarizer was used to obtain polarization-resolved near-field pat-
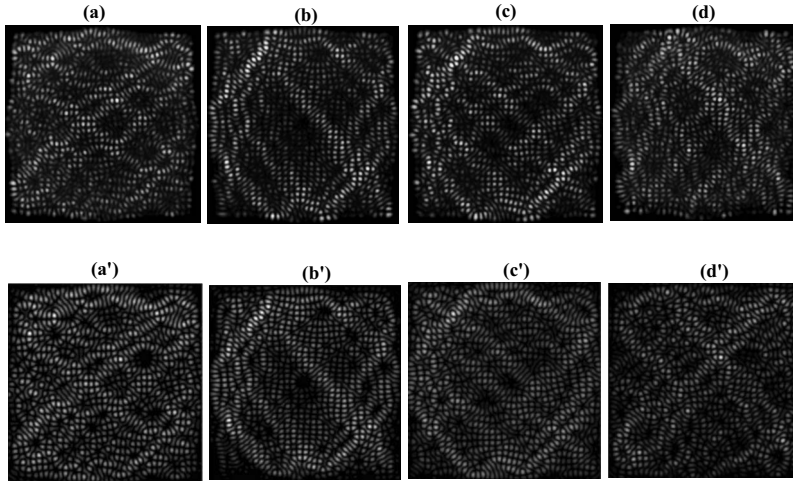
FIG. 3. Experimental polarization-resolved near-field patterns observed at the operating temperature of $T=265$ K with polarization in the direction (a) 0° (perpendicular), (b) 90° (horizontal), (c) 45°, and (d) 135°. (a′)–(d′) Reconstructed patterns with the eigenfunction expansion method for experimental results shown in (a′)–(d′), respectively.

terns. The spectral information in the laser output was measured by a Fourier optical spectrum analyzer (Advantest Q8347) with a Michelson interferometer. Inasmuch as the resolution of the spectrum analyzer is 0.002 nm, transverse modes separated by ~0.07 nm in the present device could be clearly resolved.

Since the gains of two orthogonally polarized modes are generally different, the lasing mode near threshold is usually dominated by one of the linearly polarized modes. In other words, the transverse wave is a scalar field and its polarization is essentially the same for all points of the transverse plane. However, precise adjustment of the operating temperature can cause the lasing thresholds of two orthogonally polarized modes to be nearly the same. Under this circumstance, the lasing modes are generally found to be made up of two distinct chaotic wave patterns with orthogonal linear polarizations. To be precise, the lasing transverse wave is a 2D chaotic vector field and its polarization is spatially dependent. For example, the experimental near-field pattern at the operating temperature of $T=265$ K and the threshold current of $I=26.9$ mA did not display exact standing-wave morphology because of the superposition of two orthogonally polarized modes. Figures 3(a) and 3(b) show the polarization-resolved near-field patterns in the 0° and 90° directions, respectively. The polarization angle is referred to the [110] direction of the (001) GaAs crystal. The orthogonally polarized modes clearly exhibit remarkably distinct chaotic patterns. The measurement of the optical spectrum indicates that the whole experimental wave is phase synchronized to a single frequency at 806.45 nm. As a consequence, the orthogonally polarized components can mutually interfere to lead to a greatly different pattern in the polarization-resolved near-field image, as shown in Fig. 3(c) for 45° polarization and Fig. 3(d) for 135° polarization. Explicitly, the entanglement of spatial structures and polarization states leads to the formation of an optical vector field. We investigated the dependence of the 2D chaotic vector field on the operating parameters, and it turns out that the experimental vector field remains unchanged for $262.5 < T < 267.5$ K and for $26.9 < I < 27.6$ mA. The width of these ranges indicates that generation of 2D chaotic vector fields is a robust phenomenon. To our best knowledge, the present result proffers the first experimental realization of 2D chaotic vector fields in a microcavity laser. As described in the following section, the experimental chaotic vector fields can be analytically described by using the eigenfunction expansion technique to reconstruct two orthogonal-polarization near-field patterns. The reconstructed patterns are depicted in Figs. 3(a′)–3(d′) for a clear comparison. It is worthwhile to clarify that all the high-order transverse modes excited from an integrable square cavity are found to be localized on classical periodic orbits [33]. In other words, a deliberate perturbation plays an essential role for the generation of the chaotic wave modes.

III. ANALYSIS OF VECTOR SINGULARITIES FOR THE EXPERIMENTAL CHAOTIC VECTOR FIELD

Since it is not feasible to measure polarization vector fields in a straightforward way, the reconstruction of the orthogonally polarized wave functions is practically useful for analyzing the properties of vector singularities. In order to reconstruct the wave functions, we need to deduce the field point matrix $\psi(x_i, y_j)$ from the experimental intensity point matrix $|\psi(x_i, y_j)|^2$, where the indices (i,j) denote the pixel positions of the CCD camera and the total pixel number of the experimental data is 200×200. Since the nodal lines separate the positive and negative domains of the wave function, a so-called positive wave distribution $|\psi_p(x_i, y_j)|$ can be obtained by preserving the wave amplitude $|\psi(x_i, y_j)|$ for the domains with the same sign and setting the wave amplitude to zero for the domains with opposite sign [22,36]. Figures 4(a) and 4(b) depict the patterns of $|\psi_p(x_i, y_j)|$ for the two orthogonally polarized modes shown in Figs. 3(a) and 3(b), respectively. With the positive wave distribution $|\psi_p(x_i, y_j)|$, the experimental wave function $\psi(x_i, y_j)$ can be determined from [22]

$$\psi(x_i, y_j) = 2 \cdot |\psi_p(x_i, y_j)| - |\psi(x_i, y_j)|. \tag{2}$$

Since the experimental wave functions are too coarse to explore the vector singularities completely, the eigenfunction expansion technique is utilized to find analytical expressions for $\psi(x_i, y_j)$. With the eigenstates of 2D square billiards as a basis, the experimental polarization-resolved wave function can be expressed as
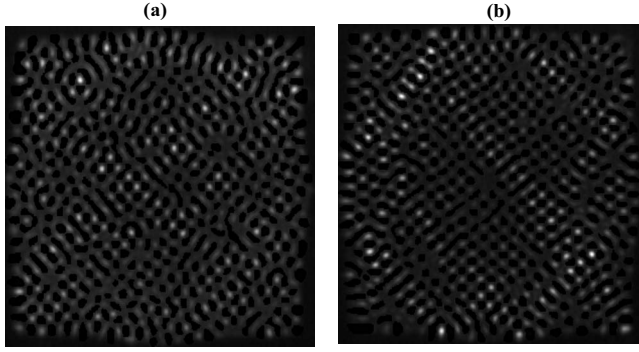
FIG. 4. (a), (b) Intensity plots of the positive wave functions $|\psi_p(x_i, y_j)|$ for experimental results shown in Figs. 3(a) and 3(b), respectively.

$$\psi(x,y) = \sum_m \sum_n C_{m,n} \sin\left(\frac{m\pi}{a}x\right)\sin\left(\frac{n\pi}{a}y\right), \qquad (3)$$

where a is the length of the square boundary, m and n are the quantum numbers in the x and y directions, respectively, and $C_{m,n}$ denote the expansion coefficients. Even though some other bases can be chosen for the expansion, the simple analytical form of the eigenstates of 2D square billiards causes the calculation to be extremely straightforward. The orthogonality relation leads $C_{m,n}$ to be

$$C_{m,n} = \int_0^a \int_0^a \psi(x,y)\sin\left(\frac{m\pi}{a}x\right)\sin\left(\frac{n\pi}{a}y\right)dx\,dy. \qquad (4)$$

With the experimental wave function $\psi(x_i, y_j)$, the integral in Eq. (4) can be numerically calculated by a summation:

$$C_{m,n} = \sum_{i=1}^N \sum_{j=1}^N \psi(x_i, y_j)\sin\left(\frac{m\pi}{a}x_i\right)\sin\left(\frac{n\pi}{a}y_j\right)\Delta x_i\,\Delta y_j. \quad (5)$$

Figures 5(a) and 5(b) show the intensity plots for $|C_{m,n}|$ for the experimental polarization-resolved modes at 0° and 90°, respectively. The distributions of $|C_{m,n}|$ are found to be specifically localized on a thin ring. It is noteworthy that the intensity distribution in Fig. 3(b) exhibits a slight scarring effect; nevertheless, its statistical properties are rather close to the characteristics of the chaotic wave function of Berry's conjecture [2], as shown in Figs. 6 and 7. With the expansion

coefficients $C_{m,n}$, we can obtain analytical wave functions for the experimental polarized-resolved modes in terms of 2D square-billiard eigenstates. Figures 3(a′) and 3(b′) depict the wave patterns of the analytical wave functions corresponding to the experimental polarization-resolved modes at 0° and 90°, respectively. It can be clearly seen that the experimental polarization-resolved patterns are well reconstructed with the analytical wave functions.

Let $\psi_x(x,y)$ and $\psi_y(x,y)$ denote the polarization-resolved wave functions at 0° and 90°, respectively. In terms of $\psi_x(x,y)$ and $\psi_y(x,y)$, the vector field distribution for the experimental pattern is given by

$$|E\rangle = \psi_x(x,y)|x\rangle + \psi_y(x,y)|y\rangle, \qquad (6)$$

where $|x\rangle$ and $|y\rangle$ are the unit vectors in the x and y directions, respectively. With the vector field $|E\rangle$ the polarization-resolved wave functions at 45° and 135° are given by

$$\psi_{45}(x,y) = \frac{1}{\sqrt{2}}[\psi_x(x,y) + \psi_y(x,y)] \qquad (7)$$

and

$$\psi_{135}(x,y) = \frac{1}{\sqrt{2}}[-\psi_x(x,y) + \psi_y(x,y)]. \qquad (8)$$

Figures 3(c′) and (3d′) depict the numerical results for the intensity patterns of $|\psi_{45}(x,y)|^2$ and $|\psi_{135}(x,y)|^2$, respectively. The good agreement between the numerical and experimental patterns evidences the accuracy of the reconstructed wave function in representing the observed vector field.

To further validate that the experimental observation is a chaotic vector field, we use the reconstructed wave functions to calculate the amplitude and intensity distributions. For the chaotic wave function of Berry's conjecture, the amplitude distribution is a Gaussian function,

$$P(\psi) = \frac{1}{\sqrt{2\pi}\sigma}e^{-\psi^2/2\sigma^2}, \qquad (9)$$
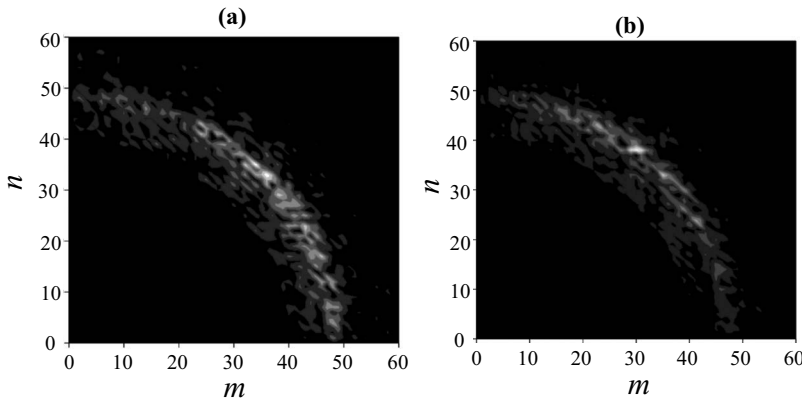

FIG. 5. (a), (b) Distribution of the coefficients $|C_{m,n}|$ obtained by Eq. (3) for experimental results shown in Figs. 3(a) and 3(b), respectively.
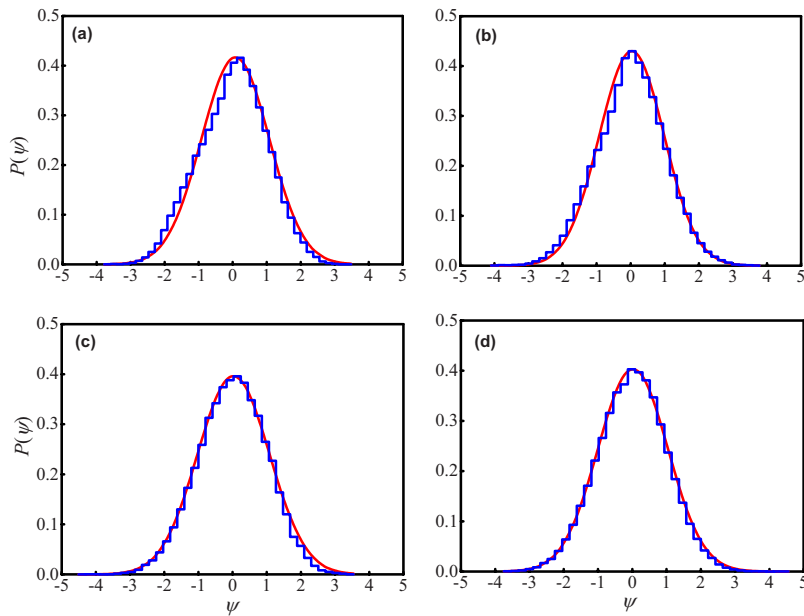
FIG. 6. (Color online) (a)–(d) Amplitude distributions of the polarization-resolved wave functions (blue stepped lines) for experimental results shown in Figs. 3(a)–3(d), respectively. Red lines: Gaussian distributions [Eq. (9)].

and the intensity distribution is shown to be a Porter-Thomas distribution

$$P(|\psi|^2) = \frac{1}{\sqrt{2\pi|\psi|^2}} e^{-|\psi|^2/2}. \tag{10}$$

Figures 6 and 7 illustrate the amplitude and intensity distributions of the polarization-resolved wave functions, respectively. All amplitude and intensity distributions of the polarization-resolved wave functions shown in Fig. 3 are

found to be in fairly good agreement with the theoretical distributions.

In addition to the chaotic modes, scarred modes related to classical periodic orbits also exist in the present ripple square billiard. Figures 8(a)–8(d) show the experimental polarization-resolved near-field patterns observed at the operating temperature of $T=210$ K. All intensity patterns can be clearly seen to be localized on the trajectories of classical periodic orbits. These findings are basically consistent with the theoretical results obtained by Li *et al.* [37] except for the characteristics of the vector field.

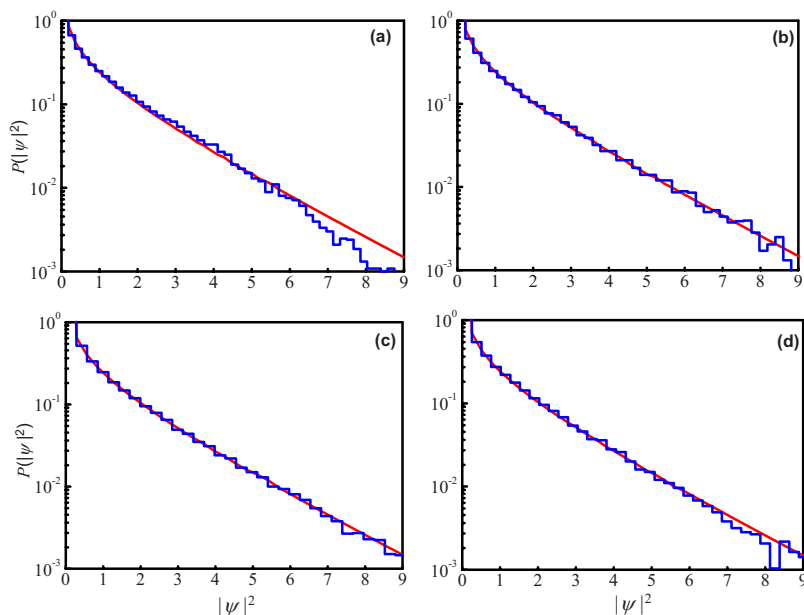The vector singularities are generally described by the angle function

FIG. 7. (Color online) (a)–(d) Intensity distributions of the polarization-resolved wave functions (blue stepped lines) for experimental results shown in Figs. 3(a)–3(d), respectively. Red lines: Gaussian distributions [Eq. (10)].
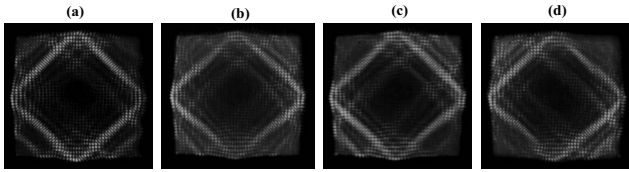
FIG. 8. Experimental polarization-resolved near-field patterns observed at the operating temperature of $T=210$ K with polarization in the direction (a) 0° (perpendicular), (b) 90° (horizontal), (c) 45°, and (d) 135°.

$$\Theta(x,y) = \arctan\left(\frac{\psi_y(x,y)}{\psi_x(x,y)}\right). \tag{11}$$

The vortices of the angle function $\Theta(x,y)$ correspond to the vector singularities at which the orientation of the electric field vector is undefined. Figure 9(a) depicts the numerical pattern of the angle function $\Theta(x,y)$ for the experimental vector field. Here the angle is color coded (gray scaled) and the singularities are at the points where all colors come together. The polarization vector field is clearly seen to reveal a highly sophisticated interlace pattern. A small region of the vector field is depicted in Fig. 9(b) to demonstrate the minute features of the vector singularities.

It is of pedagogical importance to confirm the sign rule that the nearest-neighbor singularities on any contour of constant phase are required to have opposite signs [38]. Figure 9(c) illustrates the zero-crossing map of $\psi_x(x,y)$ and $\psi_y(x,y)$ for the square region shown in Fig. 9(b). All saddle points are manifestly found to be open saddles with no joined arms. In other words, no closed saddles are found in the experimental vector field and no phase extrema are observed. This result is consistent with the theoretical analysis that the phase extrema are really rare because there is little room left in the phase field to accommodate them [38].

IV. CONCLUSION

Previously, we manufactured a square-shaped VCSEL device with a moderate ripple boundary to investigate the statistical properties of chaotic wave functions in a nonintegrable system [22]. In the present work, the same laser device has been utilized to generate 2D chaotic vector fields by means of precisely controlling the operating temperature and operating current. The 2D chaotic vector field was found to be composed of two linearly polarized laser modes with different chaotic spatial structures, but synchronized to a single frequency. The eigenfunction expansion technique has been employed to reconstruct the wave function for each orthogonal polarization near-field pattern to explore the properties of vector singularities. The numerical analysis verifies the sign rule that the nearest-neighbor singularities on any contour of constant phase have opposite signs in the phase space of the vector field. It is also confirmed that phase extrema are scarcely visible in 2D chaotic vector fields.

Recently, we studied the polarization singularities of 2D regular vector fields in a standard spherical laser cavity that
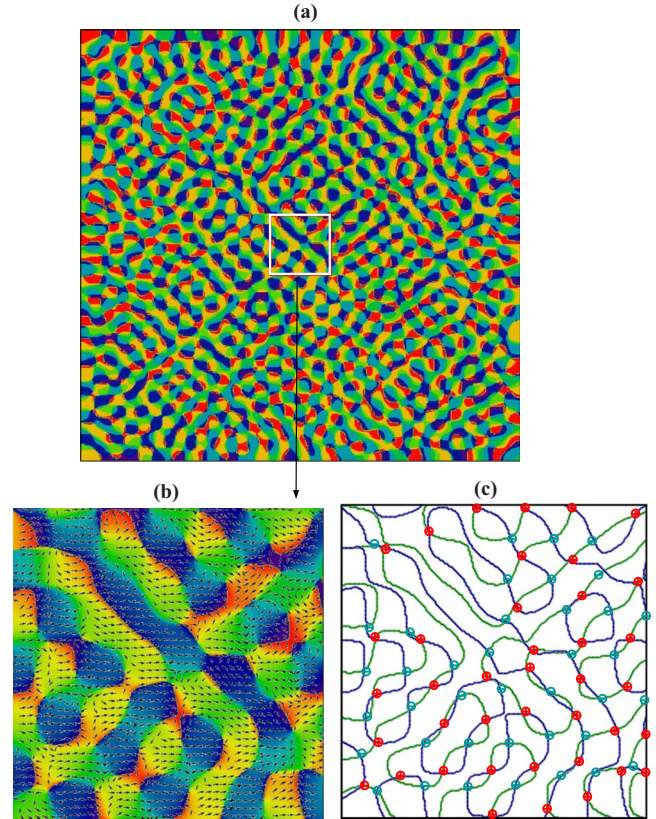

FIG. 9. (Color online) (a) Numerical pattern of the angle function $\Theta(x,y)$ for the experimental vector field. (b) Zoomed view of the angle field $\Theta(x,y)$. The arrows display the normalized vector field distributions. (c) Zero-crossing map of $\psi_x(x,y)$ and $\psi_y(x,y)$ for the square region shown in (b): positive and negative index singularities indicated by their signs + and −, respectively.

is an integrable system with the transverse confinement equivalent to an isotropic 2D harmonic oscillator [34,39]. Here we have generated and investigated the polarization singularities of 2D chaotic vector fields in a surface-emitting microcavity that is a nonintegrable system with the transverse confinement equivalent to a 2D rigid wall. As expected, the distributions of the polarization singularities are quite different for these two distinct paraxial laser cavities. However, experimental results and theoretical analyses reveal that phase extrema do not exist in the general 2D paraxial vector fields no matter whether they are regular or chaotic. Therefore, the conditions of existence of the phase extrema deserve further study.

ACKNOWLEDGMENTS

[1] H. J. Stöckmann, *Quantum Chaos: An Introduction* (Cambridge University Press, Cambridge, U.K., 1999), and references cited therein.

[2] M. V. Berry, J. Phys. A **10**, 2083 (1977).

[3] E. J. Heller, Phys. Rev. Lett. **53**, 1515 (1984).

[4] P. O'Connor, J. Gehlen, and E. J. Heller, Phys. Rev. Lett. **58**, 1296 (1987).

[5] S. W. McDonald and A. N. Kaufman, Phys. Rev. A, **37**, 3067 (1988).

[6] Katsuhiro Nakamura and Takahisa Harayama, *Quantum Chaos and Quantum Dots* (Oxford University Press, New York, 2004), and references cited therein.

[7] K. F. Berggren, A. F. Sadreev, and A. A. Starikov, Phys. Rev. E **66**, 016218 (2002).

[8] K. N. Pichugin and A. F. Sadreev, Phys. Rev. B **56**, 9662 (1997).

[9] I. V. Zozoulenko, R. Schuster, K. F. Berggren, and K. Ensslin, Phys. Rev. B **55**, R10209 (1997).

[10] J. P. Bird, R. Akis, D. K. Ferry, D. Vasileska, J. Cooper, Y. Aoyagi, and T. Sugano, Phys. Rev. Lett. **82**, 4691 (1999).

[11] R. Crook, C. G. Smith, A. C. Graham, I. Farrer, H. E. Beere, and D. A. Ritchie, Phys. Rev. Lett. **91**, 246803 (2003).

[12] S. Sridhar, Phys. Rev. Lett. **67**, 785 (1991).

[13] J. Stein and H. J. Stöckmann, Phys. Rev. Lett. **68**, 2867 (1992).

[14] A. Kudrolli, V. Kidambi, and S. Sridhar, Phys. Rev. Lett. **75**, 822 (1995).

[15] Y. H. Kim, M. Barth, H. J. Stöckmann, and J. P. Bird, Phys. Rev. B **65**, 165317 (2002).

[16] P. A. Chinnery and V. F. Humphrey, Phys. Rev. E **53**, 272 (1996).

[17] A. Kudrolli, M. C. Abraham, and J. P. Gollub, Phys. Rev. E **63**, 026208 (2001).

[18] V. Doya, O. Legrand, F. Mortessagne, and C. Miniatura, Phys. Rev. Lett. **88**, 014102 (2001).

[19] Y. F. Chen, K. W. Su, T. H. Lu, and K. F. Huang, Phys. Rev. Lett. **96**, 033905 (2006).

[20] K. F. Huang, Y. F. Chen, H. C. Lai, and Y. P. Lan, Phys. Rev. Lett. **89**, 224102 (2002).

[21] T. Gensty, K. Becker, I. Fischer, W. Elsäßer, C. Degen, P. Debernardi, and G. P. Bava, Phys. Rev. Lett. **94**, 233901 (2005).

[22] C. C. Chen, C. C. Liu, K. W. Su, T. H. Lu, Y. F. Chen, and K. F. Huang, Phys. Rev. E **75**, 046202 (2007).

[23] Y. F. Chen, K. F. Huang, H. C. Lai, and Y. P. Lan, Phys. Rev. E **68**, 026210 (2003).

[24] J. F. Nye, Proc. R. Soc. London, Ser. A **387**, 105 (1983).

[25] M. S. Soskin, V. G. Denisenko, and R. I. Egorov, J. Opt. A, Pure Appl. Opt. **6**, S281 (2004).

[26] M. V. Berry, J. Opt. A, Pure Appl. Opt. **6**, 475 (2004).

[27] M. S. Soskin and M. V. Vasnetsov, Prog. Opt. **42**, 219 (2000).

[28] I. Freund, Opt. Commun. **199**, 47 (2001).

[29] L. Gil, Phys. Rev. Lett. **70**, 162 (1993).

[30] T. Erdogan, Appl. Phys. Lett. **60**, 1921 (1992).

[31] F. Prati, G. Tissoni, M. S. Miguel, and N. B. Abraham, Opt. Commun. **143**, 133 (1997).

[32] I. V. Veshneva, A. I. Konukhov, L. A. Melnikov, and M. V. Ryabinina, J. Opt. B: Quantum Semiclassical Opt. **3**, S209 (2001).

[33] Y. F. Chen, K. F. Huang, H. C. Lai, and Y. P. Lan, Phys. Rev. Lett. **90**, 053904 (2003).

[34] Y. F. Chen, T. H. Lu, and K. F. Huang, Phys. Rev. Lett. **96**, 033901 (2006).

[35] N. Shvartsman and I. Freund, Phys. Rev. Lett. **72**, 1008 (1994).

[36] N. Savytskyy, O. Hul, and L. Sirko, Phys. Rev. E **70**, 056209 (2004).

[37] W. Li, L. E. Reichl, and B. Wu, Phys. Rev. E **65**, 056220 (2002).

[38] I. Freund, Phys. Rev. E **52**, 2348 (1995).

[39] T. H. Lu, Y. F. Chen, and K. F. Huang, Phys. Rev. E **75**, 026614 (2007).